Canadian Geotechnical Journal

Research Article

Runup and impact load of debris-flow oblique shocks on deflection barrier: theoretical models and experimental verification

Yunhui Liu[a,b], **Dongri Song**[a], **Jia Liu**[a,c,d], **and Lei Feng**[a,e]

[a]Institute of Mountain Hazards and Environment, Chinese Academy of Sciences, Chengdu, China; [b]University of Chinese Academy of Sciences, Beijing, China; [c]School of River and Ocean Engineering, Chongqing Jiaotong University, Chongqing, China; [d]Urban Geological Survey and Monitor Institute of Hunan Province, Changde, China; [e]Patent Examination Cooperation Sichuan Center of the Patent Office, CNIPA, Chengdu, China

Corresponding author: **Dongri Song** (email: drsong@imde.ac.cn)

Abstract

Deflection barriers are often constructed to divert debris flows to less hazardous areas, where oblique shocks form upon impact. This study presents theoretical models for oblique shock against a deflection barrier, which predicts the runup height and impact load of oblique shocks with known incoming-flow conditions. Flume experiments are then conducted with the flume inclination and gate opening height as variables to quantify the incoming flow conditions via the Froude number, and to validate the performance of the oblique shock model. The experimental results show that both runup height and impact load (in dimensionless form) increase with the incoming-flow Froude number, which is well predicted by the theoretical models. The runup height and impact load of normal shocks can be considered as upper limits of oblique shocks. However, it would be overly conservative to adopt the predicted runup and impact load of normal shocks for oblique-shock mitigation. It should be noted that the proposed model is not applicable in scenarios where dead zones form between the deflected flows. Findings of this study lay a theoretical foundation for the design of mitigation structures aimed at diverting debris flows.

Key words: debris flow, oblique shock, runup height, impact load, theoretical model

Résumé

Les barrières de déflexion sont souvent construites pour détourner les coulées de débris vers des zones moins dangereuses, où des chocs obliques se forment lors de l'impact. Cette étude présente des modèles théoriques pour les chocs obliques contre une barrière de déflexion, qui prédisent la hauteur de levée et la charge d'impact des chocs obliques avec des conditions d'écoulement entrant connues. Des expériences en canal sont ensuite menées avec l'inclinaison du canal et la hauteur d'ouverture de la vanne comme variables pour quantifier les conditions d'écoulement entrant via le nombre de Froude, et pour valider la performance du modèle de choc oblique. Les résultats expérimentaux montrent que la hauteur de levée et la charge d'impact (sous forme adimensionnelle) augmentent avec le nombre de Froude entrant, ce qui est bien prédit par les modèles théoriques. La hauteur de levée et la charge d'impact des chocs normaux peuvent être considérées comme des limites supérieures des chocs obliques. Cependant, il serait trop conservateur d'adopter la hauteur de levée et la charge d'impact prédites des chocs normaux pour atténuer les chocs obliques. Il convient de noter que le modèle proposé ne s'applique pas aux scénarios où des zones mortes se forment entre les flux déviés. Les résultats de cette étude jettent les bases théoriques de la conception de structures d'atténuation visant à détourner les coulées de débris.

Mots-clés : coulée de débris, choc oblique, hauteur de levée, charge d'impact, modèle théorique

1. Introduction

Debris flow is a devastating natural hazard in mountainous regions. Damage caused by debris flows to downstream populations and critical infrastructure can be effectively prevented or mitigated by engineering structures, such as interception or deflection barriers in the flow path (Hungr et al. 1984; Cui et al. 2007; Faug 2015; Choi et al. 2016; Liu et al. 2024). Based on the angle of deflection, debris-flow shocks can be classified as normal shocks (90° between the directions of incoming-flow and the obstacle) and oblique shocks (less than 90°). The normal shocks can be regarded as a special case of the prevalent oblique shocks. Figure 1 shows a typical debris-flow oblique shock that is induced by a rock ridge into the channel. The incoming-flow Froude number for this oblique

Fig. 1. Debris-flow oblique shock occurred on 23 July 2019 in Jiangjia Ravine, Yunnan, China: (*a*) plan view of the natural settings with a rock ridge into the channel; (*b*) a typical oblique shock due to the deflection of rock ridge, viewing from downstream to upstream.

Fig. 2. Schematic diagram (profile view) of momentum-jump model for normal shocks, where h_1 is the incoming-flow height; v_1 is the incoming-flow velocity; h_2 is the run-up height; and v' is the reflected shock-wave velocity.

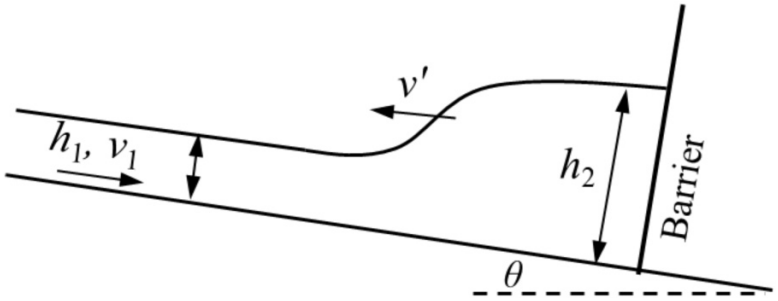

shock is approximately 2.5–3.0, and the deflection angle is 43°. The video of the whole process can be found in Supplementary B1 (https://youtu.be/6GQUBHfEEg8).

Current research on debris flow-barrier (obstacle) interaction mainly focuses on normal shocks (Ng et al. 2022, 2024; Song et al. 2023; Nagl et al. 2024). The momentum-jump model for normal shock has been well established (Faug 2021; Wu et al. 2023). The model considers the reflected shock wave induced by a stationary barrier, and the shock wave moves in the upstream direction. By establishing the mass and momentum conservation equations across the jump and assuming a static pressure distribution behind the reflected shock wave (Fig. 2), the normalized runup height h_2/h_1 of the reflected wave can be obtained (Song et al. 2021*a*, 2021*b*):

$$(1)\qquad \left(\frac{h_2}{h_1}\right)^2 - \left(\frac{h_2}{h_1}\right) - 1 + \left(\frac{h_2}{h_1}\right)^{-1} - 2Fr_1^2 = 0$$

where h is the flow depth, subscript 1 represents the pre-jump (in-coming) condition, subscript 2 represents the post-jump condition, and Fr is the Froude number:

$$(2)\qquad Fr = \frac{v}{\sqrt{gh\cos\theta}}$$

where v is the flow velocity, g is the gravitational acceleration, and θ represents the slope inclination. The normal-shock impact load F on barrier can be expressed (Albaba et al. 2018; Faug 2021):

$$(3)\qquad F = \rho v_1 h_1\left(v_1 + \frac{h_1 v_1}{h_2 - h_1}\right) + \frac{1}{2}\rho g h_1^2\cos\theta = \frac{1}{2}\rho g h_1^2\cos\theta\left[2Fr_1^2\frac{h_2/h_1}{h_2/h_1 - 1} + 1\right]$$

where v_1 is the incoming flow velocity, and ρ is the flow density.

In terms of oblique shocks (Rericha et al. 2001), current research mainly focuses on the runup behavior. Hákonardóttir and Hogg (2005) investigated the physical processes of oblique shocks using dry granular and water flows. Under steady deflection, the granular flow regime changed abruptly across the oblique shock, resulting in variation in depth, velocity, and direction, which shares similarities with those of water flows. Through flume model tests, Faug et al. (2007) found that the hydraulic Bélanger formula (see eq. 4) is equally effective in predicting oblique runup height of dry granular flows like avalanches. By adjusting the flume hopper gate opening and deflection angle, Cui (2021) studied the oblique-shock wave of dry granular flows and its control factors. This result demonstrates that the magnitude of shock-wave runup is jointly controlled by the incoming-flow Froude number and deflection angle.

Fig. 3. Schematic diagrams of oblique shock: (*a*) plan view; (*b*) profile view, with its section perpendicular to the shock line.

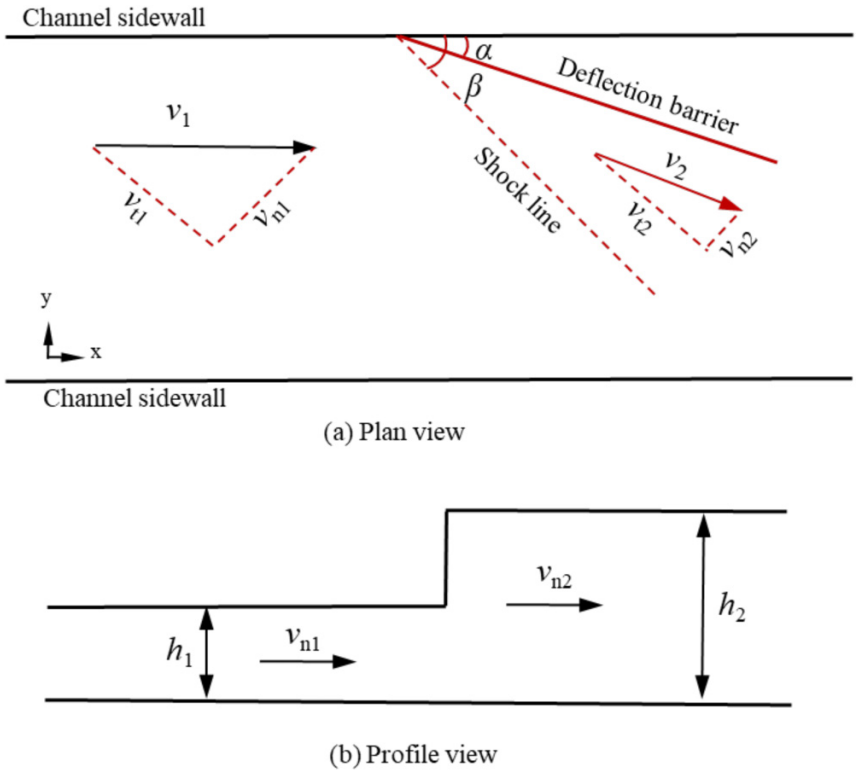

Previous studies on oblique shocks demonstrate several limitations: (1) The models for runup height only consider the flows as single-phase fluids (dry particles or water) (Hákonardóttir et al. 2003), ignoring the influence of solid–fluid interaction; (2) there is a lack of studies for estimating the impact load of oblique shocks. Debris flow is a typical two-phase material composed of both solid and liquid phases, and its internal interactions are significantly more complicated than those of dry granular flows or pure water flows. These interactions can substantially affect both runup and impact load. As shown by Song et al. (2023), the presence of solid-fluid coupling in debris flows may result in greater impact loads than those generated by either dry sand or water alone. Therefore, it is essential to consider solid–fluid interactions in our modelling framework. As a result, there is a lack of design basis for mitigation structures of debris-flow oblique impact. Since the momentum carried by the flow is fully resisted by the barrier in normal-shock models, it would be conservative to design deflection barriers using the normal-shock models.

In this study, we propose a theoretical impact-load model for oblique shocks by considering the incoming-flow condition and deflection angle. The model further takes into account the effects of shock angle and range of shock wave. Compared to the classical Bélanger equation, our model accounts for the two-phase nature of debris flows, where liquefaction directly affects the earth pressure coefficient and, consequently, the predicted runup height. The introduction of k allows the model to capture solid–liquid interactions more accurately. The existing oblique-shock runup model (Hákonardóttir and Hogg 2005; Cui 2021) is modified considering the degree of liquefaction. Our study integrates this concept by incorporating the earth pressure coefficient k to better reflect the dynamic characteristics of debris flows. (Song et al. 2023). The runup and impact load models are further verified through flume experiments.

2. Theoretical models for oblique shocks

Typical physical processes of oblique shock under ideal test condition can be viewed in Supplementary B2 and B3 (https://youtu.be/E8gnsdfh6X8 and https://youtu.be/_YSlCx3e9Mo). The oblique shock generates hydraulic jump and shock line upon impacting deflection barrier (Fig. 3*a*). The angle between the shock line and the direction of incoming-flow is defined as shock angle β. The area covered by the shock line and the deflection barrier is affected by the oblique shock. Within this area, the flow depth increases, the flow velocity decreases, and the flow direction changes from the incoming-flow direction to the direction parallel to the deflection barrier (Chanson 2004; Hákonardóttir and Hogg 2005; Faug et al. 2007; Cui 2021).

In view of the complexity of physical processes, the model of oblique shocks has to be simplified: (1) assume a uniform distribution of flow velocity across the shock (Albaba et al. 2018); (2) the fluid density remains unchanged across the shock (Chen et al. 2024); (3) the earth pressure coefficients across the shock remain the same; (4) the hydraulic jump is an abrupt process without a transitional phase (Faug 2021), which means the interface across the jump is infinitely thin (Fig. 3*b*). The scenario of simplified model is shown in Fig. 3*a*,

and the hydraulic jump profile perpendicular to the shock line is shown in Fig. 3*b*, where the *x* direction is parallel to the incoming flow, and *y* direction is perpendicular to the incoming flow. Parameters α and β represent the deflection angle and shock angle, respectively. The subscript *t* represents the tangential component of flow velocity along the shock line, and subscript *n* represents the vertical component of flow velocity.

2.1. Model for runup height

The runup of debris-flow normal shock is similar to a hydraulic jump. The hydraulic-jump process involves an increase in flow depth (runup), and the Bélanger equation (eq. 4) (Chanson 2009; Mejean et al. 2017; Albaba et al. 2018) is widely used in hydrodynamics to predict the post-jump flow depth (in a dimensionless form):

$$\frac{h_2}{h_1} = \frac{1}{2}\left(\sqrt{1+8Fr_1^2}-1\right) \tag{4}$$

where *h* is the flow depth, *v* is the flow velocity, subscript 1 represents the pre-jump (incoming) condition, and subscript 2 represents the post-jump condition. The significance of eq. 4 is that, one can accurately predict the runup height by only knowing the incoming-flow condition (i.e., h_1, v_1, and Fr_1).

Note the above runup equation is based on normal-shock condition. The runup height equation for oblique shocks has to consider the effects of deflection on flow momentum. The conservation of mass is established along the direction perpendicular to the shock line (Rajaratnam 1967)

$$h_1 v_{n1} = h_2 v_{n2} \tag{5}$$

The conservation of momentum is established across the pre-jump and the post-jump sections

$$k\frac{\rho g}{2}\cos\theta\cdot\left(h_2^2-h_1^2\right) = \rho h_1\cdot v_{n1}\left(v_{n1}-v_{n2}\right) \tag{6}$$

where *k* is the earth pressure coefficient. From the geometric relationship

$$v_{n1} = v_1\sin\beta \tag{7}$$

where β is the shock angle.

Substituting eqs. 6 and 7 into eq. 4 yields the following equation:

$$\frac{h_2}{h_1} = \frac{1}{2}\left[\sqrt{1+8k(Fr_1\sin\beta)^2}-1\right] \tag{8}$$

Compared to the traditional Bélanger equation (eq. 4), eq. 8 takes into account of the effect of two-phase solid–fluid interaction by introducing an earth pressure coefficient *k* (Song et al. 2023). According to eq. 8, the normalized runup increases with shock angle β. The addition of $\sin\beta$ to the Froude number term indicates that, compared to a normal shock, only a fraction of the momentum in oblique shock is involved in the momentum conversion (Yu and Chu 2023). The shock angle β is a function of the deflection angle α and incoming-flow Froude number Fr_1 (Ippen 1951; Gray and Cui 2007; Cui 2021):

$$\sin\beta = \frac{1}{Fr_1}\sqrt{\frac{1}{2}\frac{\tan\beta}{\tan(\beta-\alpha)}\left[1+\frac{\tan\beta}{\tan(\beta-\alpha)}\right]} \tag{9}$$

It should be noted that eq. 9 is an implicit formulation and is only applicable to oblique shocks with relatively high Froude numbers or small deflection angles (Cui et al. 2007; Gray and Cui 2007; Cui 2021). For further details on the applicable range of this equation, please refer to Fig. A1. When eq. 9 is not applicable, we propose empirical relationships for predicting the shock angle based on experimental trends. In this way, the runup height of a debris-flow oblique shock can be predicted with known incoming-flow conditions and deflection angle. The prediction of shock angle β will be further discussed in details in Section 6.2.

2.2. Model for impact load

2.2.1. The control volume of oblique shock

As shown in Fig. 4*a*, the volume (area) affected by oblique shock is taken as the control volume for force analysis. The shock begins at the initial point of contact with the deflection barrier and extends downstream along the shock line until the shock wave boundary (see Fig. 4*a*), beyond which the flow is not affected by the shock. By connecting the downstream end point of the deflection barrier through this point, a closed triangular control volume is formed with these three points, where *D* is the projected length of the control volume in the incoming-flow direction, representing the range of shock wave; *L* is the length of deflection barrier. To simplify the derivation of impact load in Section 2.2.2, dimensionless parameters D' and D'' (ratio of the geometric length scales of control volume to shock wave range) are introduced (Fig. 4*a*)

$$D' = \frac{D - L\sin\alpha}{D} \tag{10}$$

$$D'' = \frac{L\cos\alpha - \frac{D}{\tan\beta}}{D} \tag{11}$$

2.2.2. Impact load of oblique shock

The control volume is subjected to several forces on the plane of channel bed (Fig. 4*b*). The upstream hydrostatic force is defined as P_1

$$P_1 = \frac{1}{2}k\rho g h_1^2\cos\theta\cdot\frac{D}{\sin\beta} \tag{12}$$

The downstream hydrostatic force is defined as P_2

$$P_2 = \frac{1}{2}k\rho g h_2^2\cos\theta\cdot\sqrt{D'^2+D''^2} \tag{13}$$

The downslope component of the gravity of control volume G_θ

$$G_\theta = \frac{1}{2}\rho g h_2 L\cdot\left(\cos\alpha-\frac{\sin\alpha}{\tan\beta}\right)\cdot\sin\theta \tag{14}$$

Fig. 4. Schematic diagram for impact load: (*a*) plan view of control volume (by red lines); (*b*) forces acting on the control volume.

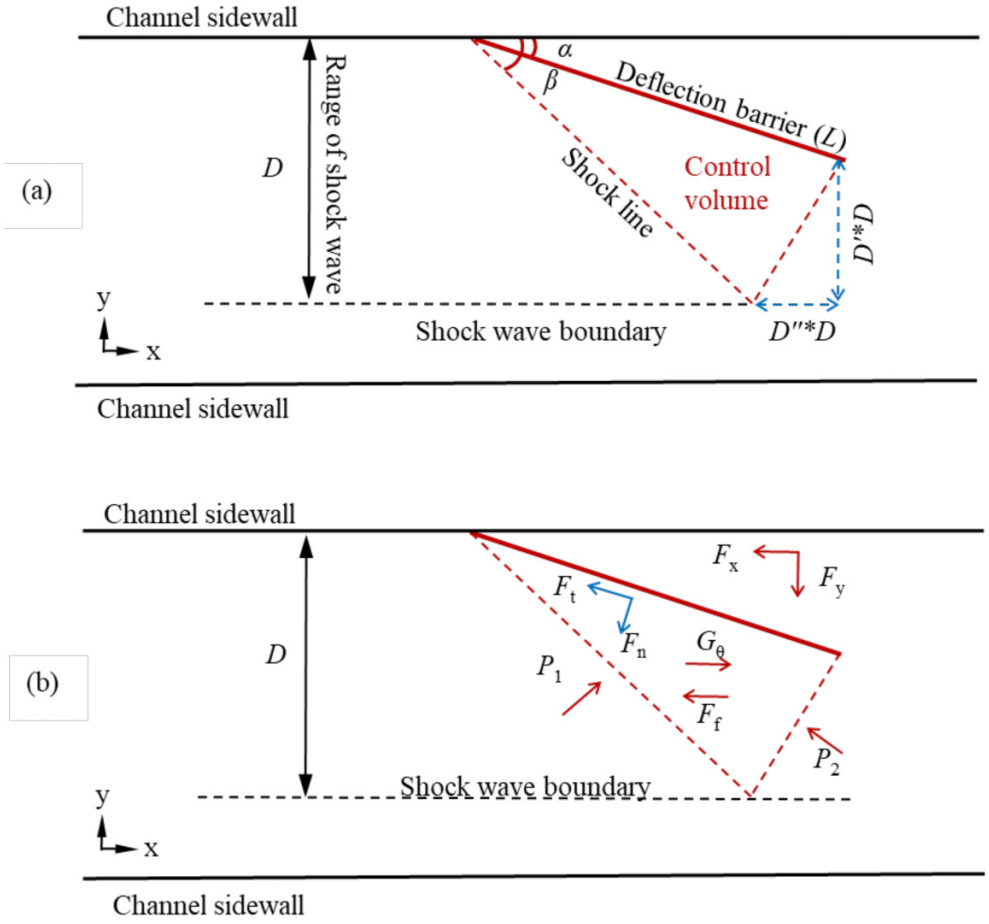

Friction at channel bed F_f

$$(15)\quad F_f = \frac{1}{2}\rho g h_2 L \cdot \left(\cos\alpha - \frac{\sin\alpha}{\tan\beta}\right) \cdot \cos\theta \cdot \mu \cdot (1-\lambda)$$

where μ is the coefficient of friction between flow and channel bed; and λ is the degree of liquefaction of two-phase flow. Along directions of incoming flow (*x*-axis) and perpendicular to incoming flow (*y*-axis), decomposing the forces of deflection barrier on the control volume as well as P_1 and P_2 yields F_x, F_y, P_{1x}, P_{1y}, P_{2x}, and P_{2y}. Based on conservation of momentum

$$(16a)\quad F_x = P_{1x} - P_{2x} + G_\theta - F_f + \rho h_1 D v_1^2 - \rho h_2 D D' v_2^2$$
$$= \frac{1}{2}k\rho g h_1^2 \cos\theta D\left\{1 - \left(\frac{h_2}{h_1}\right)^2 D' + \frac{2}{k}Fr_1^2 - \frac{2}{k}Fr_2^2\cos^2\alpha D'' + \frac{1}{k}\frac{L}{h_1}\frac{h_2}{h_1}\left(\cos\alpha - \frac{\sin\alpha}{\tan\beta}\right)[\cos\theta - \mu(1-\lambda)]\right\}$$

$$(16b)\quad F_y = P_{1y} - P_{2y}$$
$$= \frac{1}{2}k\rho g h_1^2 \cos\theta D\left[\frac{1}{\tan\beta} + \left(\frac{h_2}{h_1}\right)^2 D'' - \frac{2}{k}\left(\frac{h_2}{h_1}\right)^2 Fr_2^2 \sin^2\alpha D''\right]$$

In these equations, F_x, F_y can be further normalized by the hydrostatic force in the incoming-flow direction ($0.5k\rho g {h_1}^2 \cos\theta D$). Equation 16*a* indicates that the *x*-axis force F_x consists of the dynamic load of incoming flow, the static load, the gravity of control volume, as well as the friction at channel bed, respectively. The dynamic load is determined by the dimensionless runup height h_2/h_1 and Fr_1. The gravity of control volume is determined by the incoming-flow depth h_1, the length of deflection barrier L, and the incoming-flow conditions Fr_1. Therefore, the dimensionless term h_1/L is introduced to reflect the contribution of the static load of the control volume. Equation 16*b* indicates that the dynamic load of incoming flow does not contribute to the impact load perpendicular to the flow direction. The *y*-axis force F_y only consists of the hydrostatic loads from upstream and downstream ends.

The impact load on barrier is the counterforce from barrier to control volume. Therefore, the normal force F_n and tangential force $F_t$of the oblique shock can be obtained by a simple transformation

$$(17a)\quad F_n = F_x \sin\alpha + F_y \cos\alpha$$

$$(17b)\quad F_t = F_x \cos\alpha - F_y \sin\alpha$$

2.2.3. Parameters of the model

The known parameters of the model include (1) the incoming-flow parameters: incoming-flow depth h_1,

incoming-flow velocity v_1, and thus Froude number Fr_1; (2) parameters related to the physical properties: earth pressure coefficient k, degree of liquefaction λ, flow bulk density ρ, and friction coefficient μ; and (3) the geometrical parameters: slope inclination θ, length of deflection barrier L, deflection angle α.

The shock angle β can be directly predicted through eq. 9. For simplicity, some fixed values are preliminarily adopted in the model verification. The prediction of shock angle β will be further discussed in Section 6.2. It is difficult to derive a theoretical solution for the range of shock wave D, because it is influenced by multiple factors such as the shock angle, incoming-flow condition, slope inclination, etc. The relationship between shock wave D and the incoming-flow condition Fr_1 can be fitted based on the experimental measurement. This relationship is further adopted as an input for the impact-load prediction (further see Section 5.2).

3. Flume experiments of oblique shocks

The proposed theoretical models are verified using small-scale flume experiments. At the same time, the mechanisms of the debris-flow oblique shock are further investigated.

3.1. Flume setup

The flume used for the experiments (Fig. 5) is featured with an adjustable inclination between 20° and 30°. The flume width is designed as 300 mm, to make sure the oblique shock would not reach the side wall, i.e., $D < 300$ mm. The sidewall is made of acrylic glass, which makes it convenient to record the runup height from the side using video cameras. The base of flume is roughened using 0.6 mm glass beads. The deflection barrier used for the experiments, with a length of 120 mm and height of 100 mm, is also made of acrylic glass. The deflection barrier is fixed to the left sidewall using a lockable hinge to deflect the incoming flow and generate oblique shocks (Fig. 5). In this study, a constant deflection angle $\alpha = 30°$ is adopted.

3.2. Instrumentation

A triaxial load cell is connected behind the deflection barrier to measure the impact loads in the direction of incoming flow (x-axis) and perpendicular to the incoming flow (y-axis). The barrier is marked with red lines at space of 10 mm. A video camera is fixed at the side of flume to record the runup height at deflection barrier (Fig. 5*b*). A high-speed camera is installed over the deflection barrier to capture the shock process and for surface velocity field through particle image velocimetry (PIV) analysis (further see Section 3.5). The resolution of the high-speed camera is 1440 ∗ 1080 and the frame rate is 220 Frames Per Second (FPS).

In front of the deflection barrier, the base of flume is instrumented with a basal sensing module (Fig. 5) which integrates a triaxial load cell as well as a pore pressure transducer (PPT). Therefore, the basal normal stress, shear stress, and pore-fluid pressure of the incoming flow can be simultaneously measured. The open end of PPT is filled with glycerol–water mixture to effectively transmit the pressure of fluid phase. The open end of the PPT is further covered by a 0.4 mm steel mesh, which isolates the pressure induced by the solid phase of debris flow (Song et al. 2021*b*). An ultrasonic sensor is installed along the left sidewall of flume, corresponding to the center line of deflection barrier, to measure the incoming-flow depth (Fig. 5). The frequency of data acquisition for the basal sensing module and ultrasonic sensor is 500 Hz.

3.3. Debris-flow material

To clearly reproduce the two-phase characteristics of debris flow, mono-size glass beads (0.6 mm in diameter, 2540 kg/m^3 in density) are used for the solid phase, and a Newtonian fluid (glycerol–water mixture) is used to simulate the liquid phase. The glycerol–water mixture was prepared with a mass ratio of 46.4% water and 53.6% glycerol. The internal friction coefficient of glass beads is determined as 0.56. Black glass beads of the same size are mixed with the transparent glass beads as tracer particles for PIV analysis.

The two-phase material is set with a volumetric solid concentration of 50%, a fluid viscosity of 0.01 Pas, and a bulk density of 1839.4 kg/m^3, which are typical debris-flow parameters. To ensure that the two-phase material is uniform, continuous mixing is carried out using a helical mixer before the material is released.

3.4. Test programs

A total of nine experiments were conducted (Table 1). Each test was carried out using a constant volume of 50 L of two-phase material. The main variables of the experiments are the incoming-flow conditions (including flow depth and flow discharge), which are controlled by the flume inclination ($\theta = 20°$, 25°, and 30°) and uplift height of the gate (20, 30, and 40 mm). The variation in incoming-flow conditions is reflected by the incoming-flow Froude number (Table 2).

3.5. PIV analysis

As a noninvasive technique, PIV is widely used for flow field analysis in complex flow regimes. In this study, PIVLAB version 2.61 (Thielicke and Sonntag 2021) is adopted to perform the PIV analysis of oblique-shock processes. The images (Fig. 6*a*) analyzed by PIV are from the high-speed camera over the deflection barrier. In the analyzed flow field, a region of 5 cm upstream the barrier, equal to the barrier width, is selected for the incoming-flow velocity (Fig. 6*b*).

The streamlines deflected by the barrier are also plotted. The shock line is drawn by the following procedures: first mark the starting point of each streamline that is affected by the oblique shock and then connect the starting points as a straight shock line (Fig. 6*c*). The shock angle β is further determined from the shock line. The distance between the sidewall and the shock wave boundary (where the streamline is a straight line parallel to incoming-flow direction) is defined as the range of shock wave D (Fig. 6*c*).

Fig. 5. Flume setup and instrumentation: (*a*) schematic diagram; (*b*) photograph of test setup; and (*c*) details of basal sensing module.

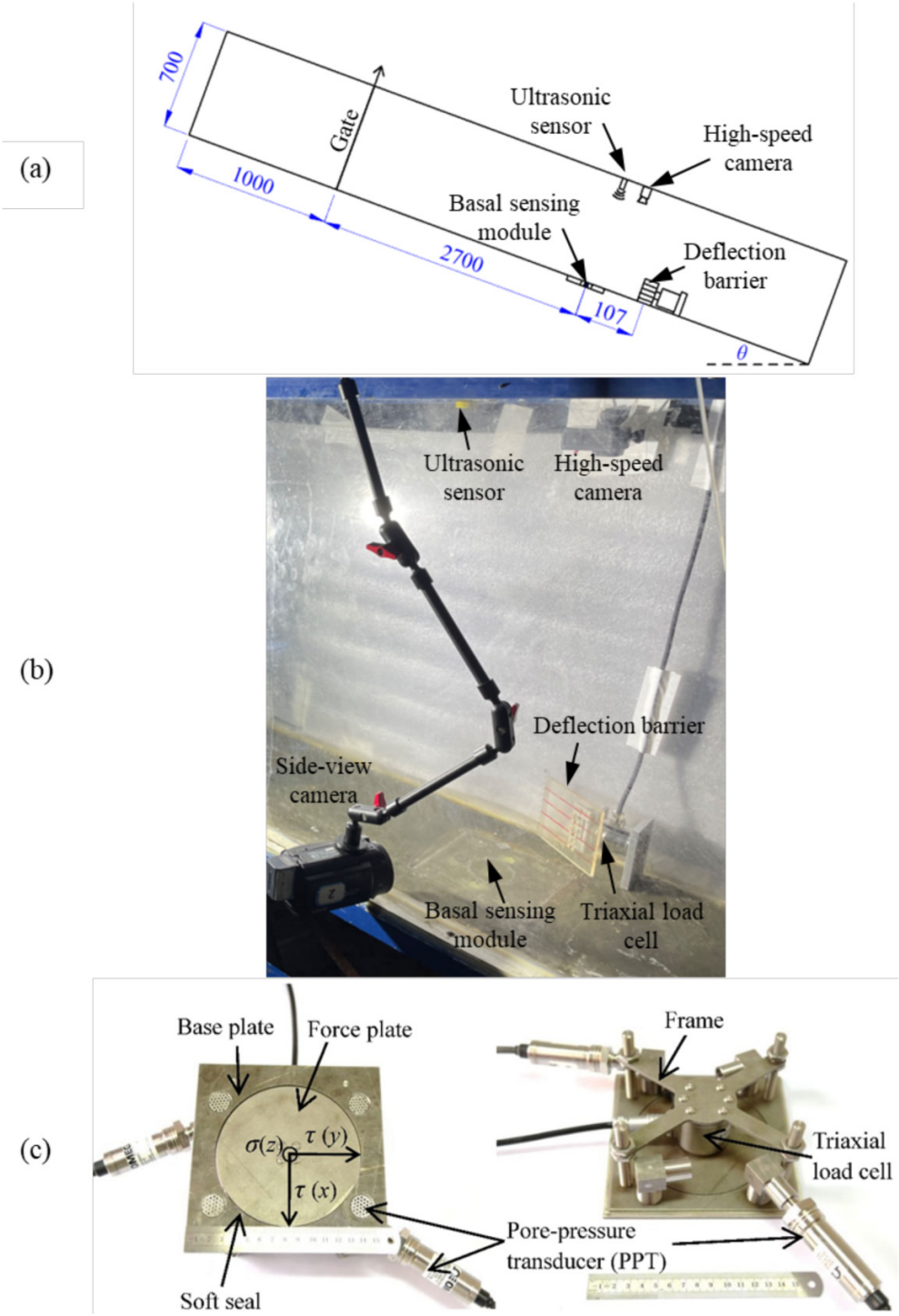

4. Experimental results

4.1. Flow regime and oblique-shock kinematics

At the beginning of the experiment, the gate are instantly lifted up to the specified height, and the debris flow started to release. After traveling a distance of 3000 mm, the flow gets fully developed. By controlling the uplift height of the gate, as well as the flume inclination, the incoming-flow Froude number for this series of experiments is within a range of 1.4–2.9 (Table 2). The experimental Fr_1 falls within the range of natural debris flows (Hübl et al. 2009).

The oblique shock of test M-25-30 is adopted here to illustrate the evolution of oblique-shock runup. Side-view and plan-view videos can be found in Supplementary B2 and B3 (https://youtu.be/E8gnsdfh6X8 and https://youtu.be/_YSlCx3e9Mo). Oblique shock (i.e., shock line and elevated flow height)

Table 1. Test program.

Test ID	Flume inclination (θ/°)	Deflection angle (α/°)	Gate uplift height (mm)
M-20-20	20	30	20
M-20-30			30
M-20-40			40
M-25-20	25		20
M-25-30			30
M-25-40			40
M-30-20	30		20
M-30-30			30
M-30-40			40

Table 2. Test results.

Test ID	Incoming-flow Froude number (Fr_1)	Incoming-flow velocity (v_1/[m/s])	Incoming-flow height (h_1/mm)	Runup height (h_2/mm)	h_2/h_1	Shock angle (β/°)	Range of shock wave (D/mm)	x-direction impact load (F_x/N)	y-direction impact load (F_y/N)
M-20-20	1.49	0.82	32	47	1.45	66	110	4.22	2.56
M-20-30	1.45	0.95	30	45	1.53	65	105	3.49	2.04
M-20-40	2.45	0.99	26	65	2.50	66	78	3.22	1.89
M-25-20	1.69	0.84	34	53	1.55	60	92	4.16	2.33
M-25-30	2.43	1.24	29	58	1.99	63	80	4.36	2.58
M-25-40	2.81	1.35	17	53	3.05	60	76	2.2	1.36
M-30-20	1.68	1.15	38	59	1.56	63	89	4.37	2.62
M-30-30	2.53	1.08	32	72	2.24	61	95	5.13	2.98
M-30-40	2.81	1.45	31	83	2.65	63	90	6.59	3.75

forms right after the incoming-flow reaches the deflection barrier (Fig. 7). At $t = 0.0$ s, the gate was lifted (Fig. 7*a*). After approximately 2.0 s, the incoming flow reached the deflection barrier, initiating the oblique shock process (Fig. 7*b*). Within 0.6 s, the flow rapidly surged upward, reaching its peak runup height—approximately two-thirds of the wall height (Fig. 7*c*). Subsequently, the runup height slightly decreased (Fig. 7*d*). In the following stage, the oblique shock entered a relatively steady phase, during which the flow trajectory along the wall became approximately parabolic, and the runup height remained stable (Figs. 7*d* and 7*e*). Finally, as the incoming flow diminished and the inflow Froude number dropped below 1 (subcritical flow regime), the runup height equaled the flow depth of the inflow (Fig. 7*f*).

4.2. Basal stresses and pore-fluid pressure

Basal stresses and pore-fluid pressure measurements at the base of flume for test M-30-30 are shown in Fig 8. Normal stress, shear stress, pore-fluid pressure, and flow depth bear similar trends for the incoming-flow, with the highest values at the front of incoming-flow and a flat decrease in response to the decreasing flow depth. The normal stress is higher than the shear stress. As the incoming-flow proceeds, the measured normal stress and pore-fluid pressure get close with each other. Under a solid concentration of 50% (lower than the critical-state concentration ~58%), the granular skeleton would contract under shear, and the pore-fluid pressure would bear the total stress. The degree of liquefaction approaches unity ($\lambda = 1$), corroborating the use of earth pressure coefficient $k = 1$ for the following calculation of impact load.

4.3. Time histories of oblique impact load

The impact load on the deflection barrier is decomposed along the direction parallel to the incoming flow (x-axis) and perpendicular to the incoming flow (y-axis). The impact-load time histories are plotted according to the flume inclination ($\theta = 20°$, $25°$, and $30°$; Fig. 9). With a higher uplift height of the hopper gate, the flow front would be steeper and faster. Therefore, the arrival time would be shorter. Meanwhile, the magnitude of the impact load is positively correlated with the uplift height of the hopper gate. Furthermore, as the flume inclination becomes steeper, the time history of the impact load is characterized with a more significant peak value.

5. Verification of theoretical models

The recorded runup height and impact load are adopted to verify the theoretical models in this section. Unlike the steady discharge of dry granular flows (Hákonardóttir and Hogg 2005; Cui 2021), it is challenging to establish steady incoming-flow conditions for two-phase flows (Song et al. 2021*b*). The transient shock impact loads (Fig. 9) and flow velocity (Fig. A2) reflect the unsteady feature of the incoming flows. Note the formation of oblique shock by the incoming flow is transient and does not depend on the history of previous shock process. In the subsequent analysis,

Fig. 6. Particle image velocimetry analysis of test M-25-30: (*a*) captured shock wave by high-speed camera; (*b*) velocity field; and (*c*) characteristics of oblique shock.

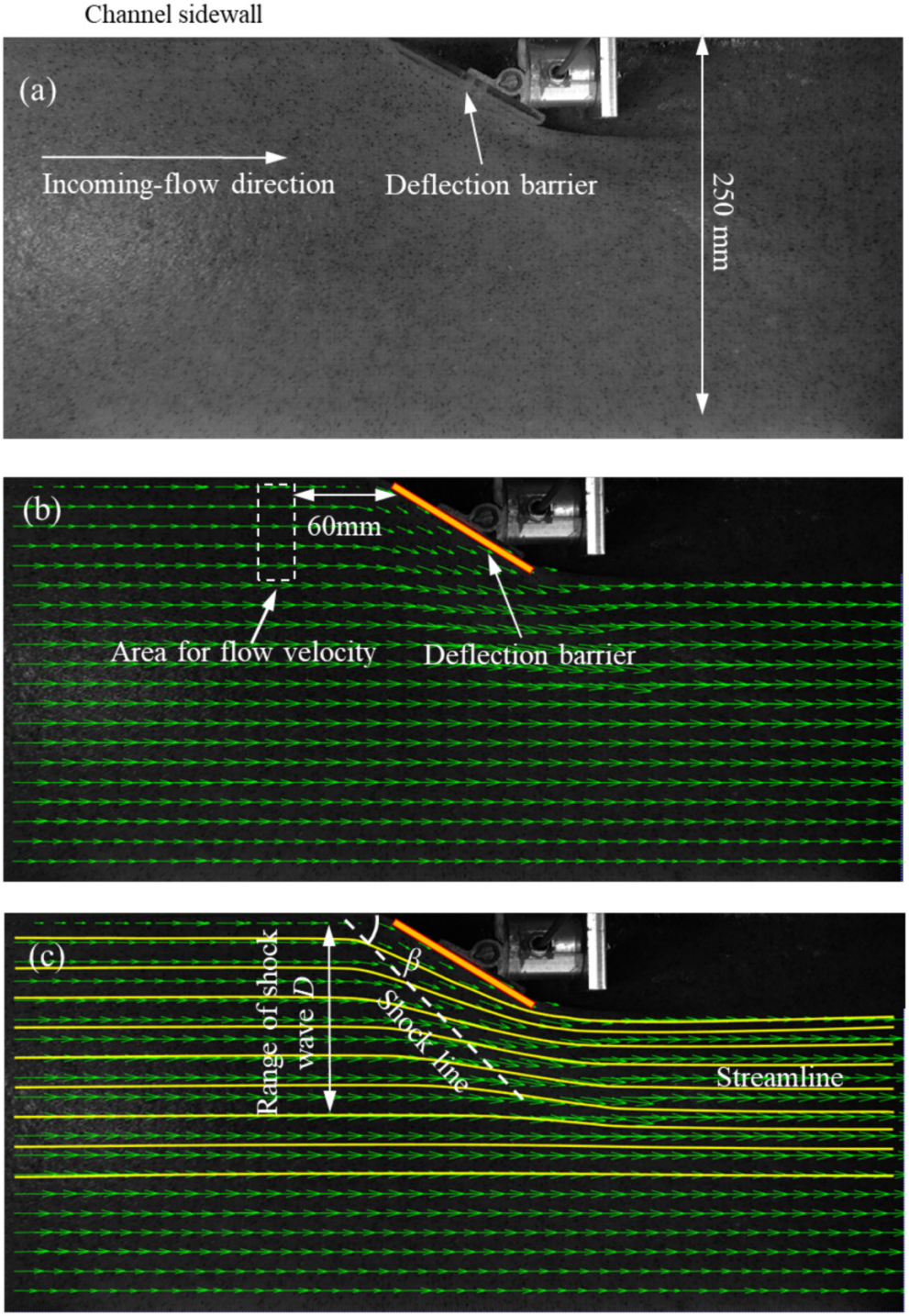

we added the peak values of the incoming flow velocity and runup height to calculate the front incoming Froude number to verify the selection of the relatively stable stage of the incoming flow and its corresponding impact response (runup height and impact load), and compared it with the incoming flow Froude number of the steady stage to verify that the steady-state measurement results are feasible. In this study, we refer to the time history of the incoming-flow velocity v_1 (Fig. A2) and choose a specific period ($\Delta t = 0.1$ s) after the front of incoming-flow where the flow velocity is relatively steady. Within this period, the flow condition is regarded as steady and average values of the velocity, runup, and impact load are adopted as characteristic parameters for model verification.

Fig. 7. The oblique impact process of experiment M-25-30: (*a*) $t = 0$ s denotes the moment when the ultrasonic sensor begins recording the incoming flow; (*b*) at $t = 2.0$ s, the flow front first makes contact with the deflection barrier; (*c*) at $t = 2.6$ s, the runup height reaches its maximum; (*d*) at $t = 3.0$ s, the runup height slightly decreases; (*e*) at $t = 6.6$ s, the runup height remains stable, indicating a quasi-steady state; and (*f*) at $t = 16.0$ s, as the incoming flow depletes, the flow transitions into a subcritical regime, and the runup height becomes equal to the incoming-flow depth.

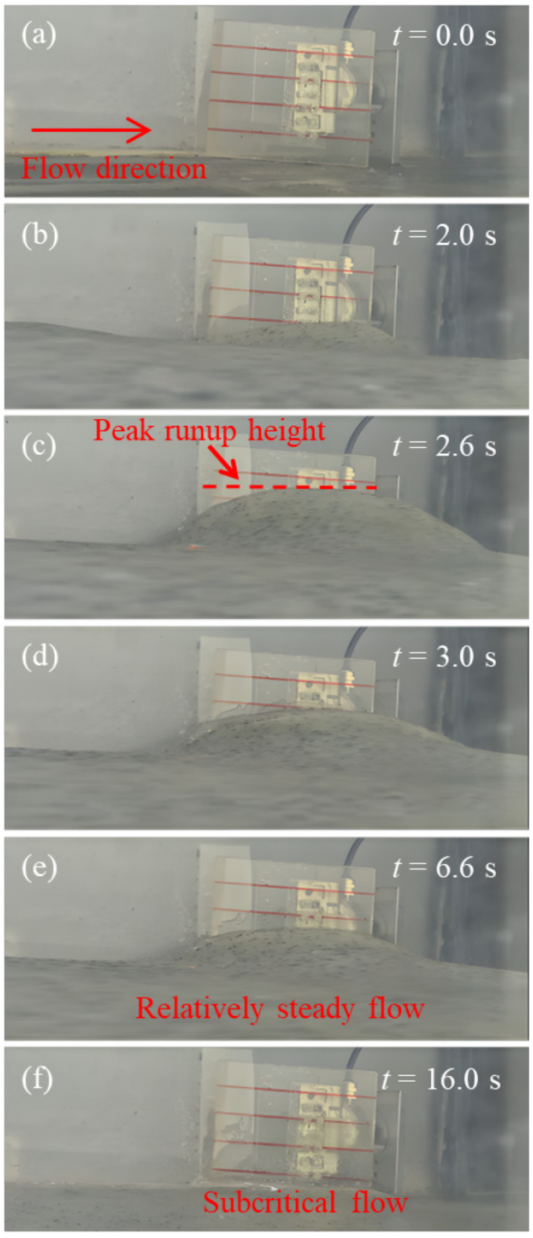

5.1. Verification of the runup height model

The characteristic parameters (h_1, v_1, k, β, Table 2) are substituted into the runup height model (eq. 8, in a dimensionless form h_2/h_1). After the front of incoming flow, the state of flows are close to fully liquefied (Fig. 8). Therefore, the value of earth pressure coefficient k is set as unity (Song et al. 2023). The dimensionless runup heights measured at the flow front (denoted by open symbols in Fig. 10) are presented alongside those obtained during the quasi-steady stage (solid symbols in Fig. 10). As illustrated, runup heights induced by the front impact are consistently lower than those observed in the steady phase. In addition, the front-impact data exhibit pronounced scatter. By contrast, the quasi-steady stage data demonstrate markedly reduced variability. Accordingly, the subsequent analysis adopts the steady-state measurements for evaluating the runup model. Since the values of shock angle β are scattered ($63^\circ \pm 3^\circ$, Table 2), the theoretical curves are plotted by setting the shock angle β as 50°, 60°, and 70°, respectively. This further verifies the sensitivity of the predicted runup height to the shock angle β. Note, shock angle β can be directly predicted through eq. 9. The prediction of the shock angle β will be further discussed in detail in Section 6.2.

Fig. 8. Stress measurement of test M-30-30 from the basal sensing module. The left vertical axis represents stress, while the right vertical axis denotes flow depth. The secondary peaks are induced by roll waves following the main surge.

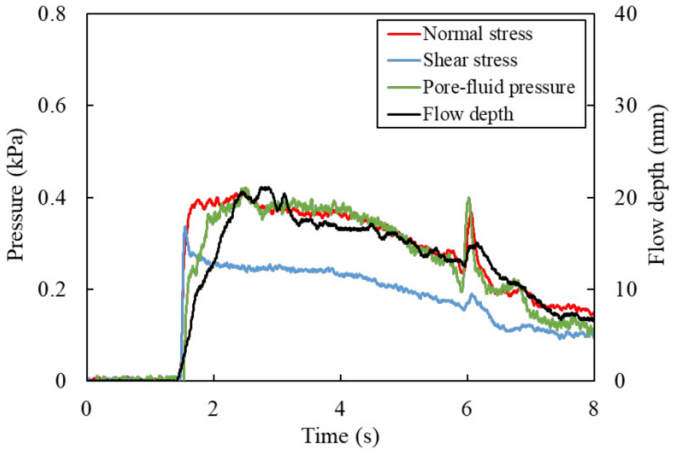

For the comparison between oblique and normal shocks, the theoretical curve of normal shock is also plotted using the momentum jump model (eq. 1). Several key findings can be highlighted by comparing these theoretical curves (Fig. 11). (1) Under the same incoming-flow conditions, the runup height of oblique shock is lower than that of normal shock. As explained in the model development (Section 2.1), only a fraction of momentum is involved in the momentum conversion of oblique shock. Therefore, the runup height of normal shocks can be regarded as the upper limit of runup height of oblique shocks. (2) The ratio h_2/h_1 rises as the incoming Froude number Fr_1 increases. (3) With constant incoming Froude number, h_2/h_1 increases with the rise of shock angle β.

The theoretical predictions are further verified against the physical measurements (Fig. 11). The measured values of h_2/h_1 are within the range between 1 and 3. As Fr_1 increases, the measured values h_2/h_1 increase correspondingly, which is consistent with the theoretical model. Within

Fig. 9. Time history of the oblique-impact load for flume inclination (*a*) $\theta = 20°$; (*b*) $\theta = 25°$; and (*c*) $\theta = 30°$. $t = 0$ s denotes opening of the gate.

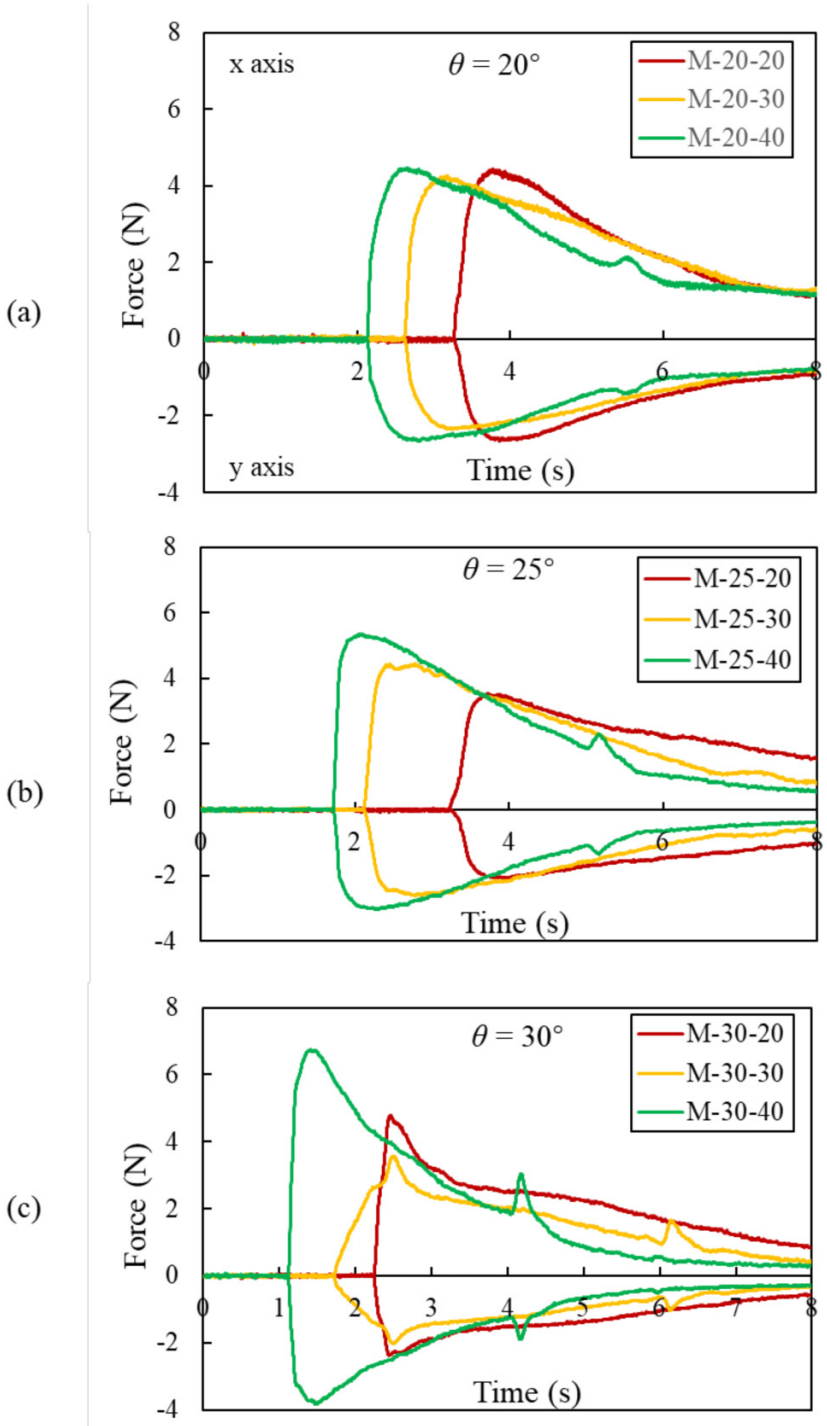

a reasonable variation of the shock angle β, the runup height model well predicts the runup height of oblique shocks with known incoming-flow conditions. The gap between the normal and oblique shock models indicates that it would be overly conservative to use the normal-shock runup model for design of oblique-shock mitigation structures.

5.2. Verification of impact-load model

The characteristic parameters (h_1, v_1, β, D, k, λ) are substituted into the impact load model (eqs. 16*a* and 16*b*) to predict the impact load in the direction of incoming-flow (x-axis) and perpendicular to the direction of incoming-flow (y-axis), respectively. Given the flows are close to liquefaction, both k and λ are set as unity. The predicted impact loads (F_x, F_y) are

Fig. 10. Comparison between theoretical predictions and physical measurements of runup height. The runup height for normal shocks is also plotted as an upper bound for oblique-shock runup. Solid symbols represent measured results during the quasi-steady stage of oblique impacts, while open symbols correspond to measurements at the flow front.

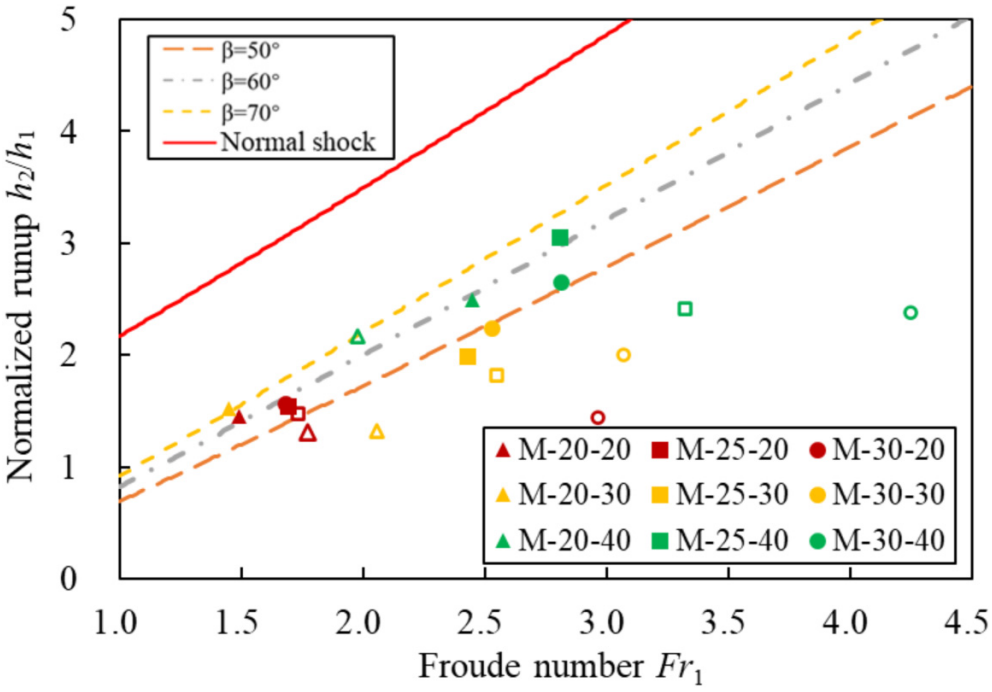

Fig. 11. Relationship between D/L and incoming-flow Froude number.

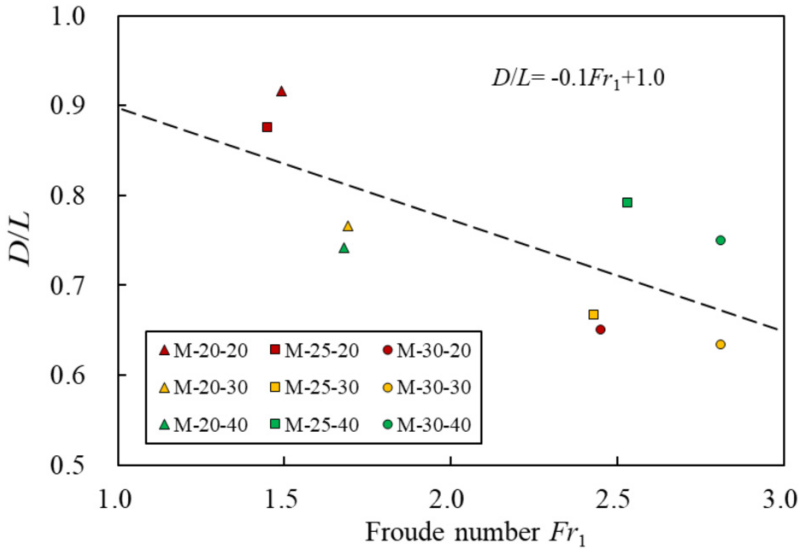

in the dimensionless form, as the ratio of impact load to the hydrostatic force in the direction of incoming flow.

Based on the measurement of flume experiments, the range of shock wave D decreases with increasing Fr_1 (Fig. 12). Therefore, the relationship between the range of shock wave D and Fr_1 is derived by using curve fitting. This relationship is further adopted as input for impact load prediction. For the predicted impact load F_x, a dimensionless term h_1/L is introduced to reflect the contribution of gravity of control volume to the impact load (eq. 16*a*). Note the incoming-flow depth h_1 and length of deflection barrier L are known parameters for the theoretical model. Nevertheless, the scattered incoming-flow depth h_1 is not convenient for model prediction. Therefore, based on the measured incoming-flow depth h_1 (Table 2), the ratio h_1/L is further set as 0.2, 0.3, and 0.4. The impact load in the perpendicular incoming-flow direction (F_y) is not affected by the gravity of control volume (eq. 16*b*).

The dimensionless impact loads measured at the flow front (represented by open symbols in Fig. 12) are plotted alongside those obtained during the quasi-steady stage (solid sym-

Fig. 12. Comparison between theoretical predictions and physical measurements of impact load: (*a*) the component in the direction of *x*-axis, where solid symbols represent the measured results of oblique shocks in the quasi-steady stage, and open symbols represent the measured front impact results; (*b*) the component in the direction of *y*-axis.

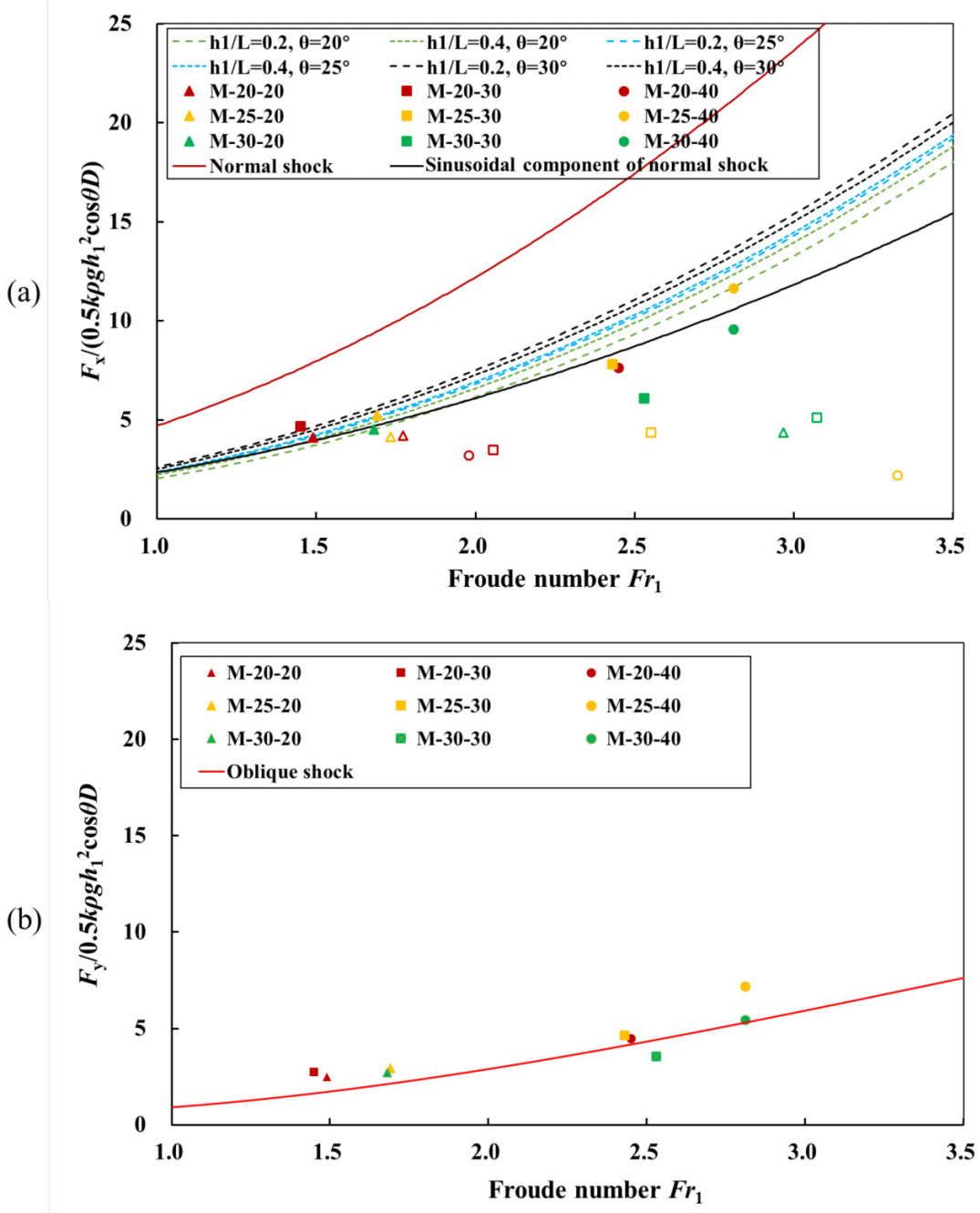

bols in Fig. 12). Similar to the runup measurement results, the impact loads associated with the front impact are generally lower than those recorded during the steady phase. Moreover, the front-impact data exhibit marked instability and significant scatter. Therefore, the dimensionless impact load measurements from the steady stage are adopted for the verification of the oblique impact-load model. The momentum jump model (impact load of normal shock, eq. 3) is used to compare the impact load of oblique shock (F_x) with that of normal shock. As expected, the normal-shock impact load is higher than that of oblique shock (Fig. 12*a*). The normal shock impact load can be regarded as the upper limit of impact load in the direction of incoming flow for oblique shocks. Within the range of h_1/L and slope inclination θ in this study, the variation of predicted impact loads is negligible. Therefore, the impact load is less affected by the gravity of control volume. The predicted impact load increases nonlinearly with the incoming-flow Froude number (Fig. 12*a*), indicating that the impact load is significantly affected by the dynamic load of incoming flows.

Fig. 13. Relationship between shock angle and incoming-flow Froude number.

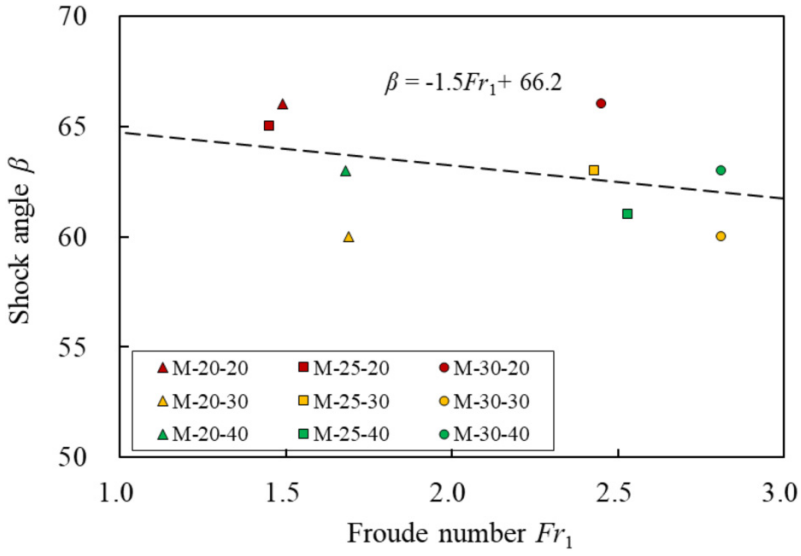

In some design guidelines, such as those implemented in Hong Kong SAR (Kwan 2012) and mainland China (China Geological Disaster Prevention Engineering Association 2018), when the barrier face is not perpendicular to the incoming flow, the impact load is taken as the sinusoidal component of the normal impact load. As shown by the black solid line in Fig. 12*a*, the sinusoidal component of the normal impact force is calculated by multiplying the right-hand side of eq. 3 with $\sin\alpha$. At lower incoming Froude numbers, our model closely matches the sinusoidal component of the normal impact load. However, as the Froude number increases, the sinusoidal component of the normal impact load is significantly lower than the predictions of our model, leading to an underestimation.

For the impact load in the direction of incoming flow (F_x), comparison between experimental measurements and theoretical predictions indicates that the experimental results are generally consistent with the model prediction, with the model prediction slightly higher in the range $Fr_1 > 2$. This could be affected by choosing characteristic parameters for the model prediction. Especially, the flow parameters under highly supercritical flow (high Fr_1) regime are subject to high degree of uncertainty.

Under a fixed deflection angle $\alpha = 30^\circ$, the magnitude of F_y is much lower than that of F_x. This is because the dynamic load of incoming flow does not contribute to the impact load perpendicular to the flow direction and F_y is only contributed by the hydrostatic loads from the upstream and downstream ends (eq. 16*b*). The prediction of impact load F_y follows a parabolic rise with the increasing incoming-flow Froude number (Fig. 12*b*). The experimental measurements agree well with the model prediction, denoting the good predictability of the model.

6. Discussion

Our model, while simplifying the treatment of oblique shock problems, has certain limitations regarding the deflection angle β and the shock range parameter D/L. The theoretical formula (eq. 9) for the shock angle β is only applicable to high Froude numbers or small deflection angles, requiring empirical relationships for low Froude numbers (Fig. 13), which reduces the general applicability of the model. Moreover, D/L, a key parameter influencing impact load prediction, is affected by multiple factors and cannot be theoretically derived. It is instead obtained through experimental fitting (Fig. 11), and its applicability and accuracy remain uncertain. Although these simplifications enhance the model's operability, they may introduce errors in practical engineering applications.

6.1. Prediction of shock angle

As shown in eq. 9, the shock angle β can be theoretically determined by the deflection angle and incoming-flow Froude number. Therefore, the shock angle can be predicted when the deflection angle and incoming-flow Froude number are known (Gray and Cui 2007; Cui 2021). However, the formula is only valid in the specific range of deflection angle and incoming-flow Froude number. For example, at deflection angle $\alpha = 30^\circ$, the formula only has solution of shock angle when incoming-flow Froude number $Fr_1 > 2.7$. Yet, below $Fr_1 = 2.7$, the experimental results demonstrate that the oblique shock would still create clear shock angle. Under this scenario, predictions may be further made using an empirical formula.

A constant deflection angle ($\alpha = 30^\circ$) is adopted in this study, so the shock angle is solely determined by the incoming-flow Froude number. By plotting the measured shock angle against the incoming-flow Froude number (Fig. 14), an empirical relationship between the shock angle and incoming-flow Froude number can be deduced. The Froude number reflects the relative magnitudes of inertial and gravitational forces. As the Froude number increases, it indicates that the inertial force dominates over the gravitational force. In oblique shock scenarios, the flow experiences strong inertial force. This force causes the flow to maintain its orig-

Fig. 14. A dead zone (detached area) formed in the experiment with deflection angle of 60°.

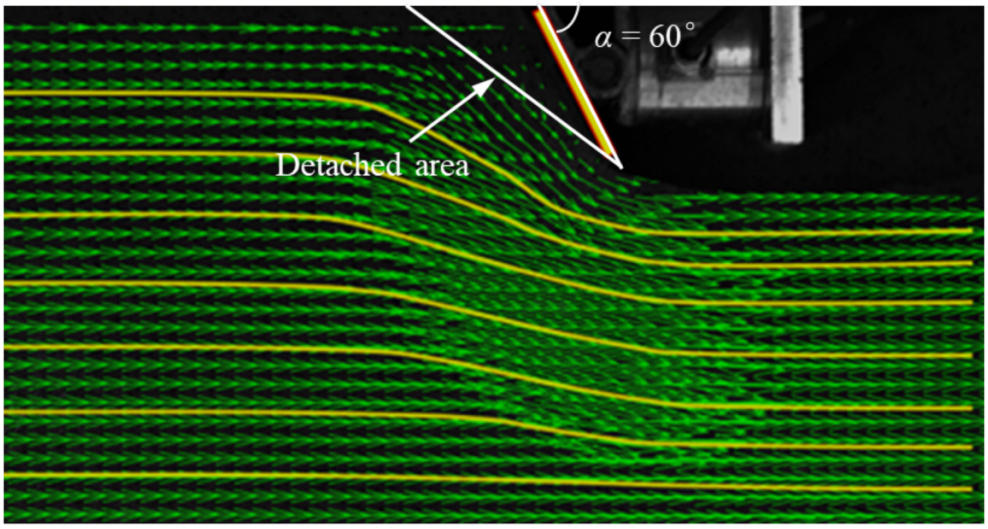

inal direction when it encounters the deflection barrier. As a result, it becomes more difficult for the barrier to significantly change the flow direction. As a result, the shock angle decreases to accommodate the stronger inertial effect, allowing the flow to adjust within a smaller angular range and continue moving forward. The shock angle decreases as the incoming-flow Froude number increases (Fig. 13). This decreasing trend aligns with the theoretical prediction (eq. 9).

6.2. Dead zone formation and the applicability of theoretical models

Besides the experiments with deflection angle of 30°, experiments with deflection angle of 45° and 60° were also carried out. In these experiments, the flow–barrier interaction generates dead zones (detached area, Fig. 14) between the barrier and deflected flow (Gray et al. 2003). The dead zone begins to form as soon as the front of incoming-flow reaches the deflection barrier. As the incoming-flow proceeds, the dead zone further expands upstream along the barrier, eventually stabilizes in an approximately triangular area. As the incoming velocity decreases, the dead zone reduces in area. Nevertheless, until the depletion of incoming flow, the dead zone remains at the corner between the barrier and sidewall.

The formation of dead zone makes it difficult to clearly define a shock angle, so the proposed theoretical models do not apply to the oblique shocks with dead zones. The generation of dead zone during oblique shocks is related to both the incoming-flow conditions and deflection angle. As supported by previous studies (Cui and Gray 2013; Khan et al. 2020, 2022; Tregaskis et al. 2022), the formation of dead zones is attributed to the combined effects of granular flow inertia, frictional resistance, and shock-wave dynamics, particularly over rough channel beds. Once a dead zone forms, the impact mechanism transitions into a bow-shaped shock, which no longer fits within the framework of conventional oblique shocks. The generation of dead zones during oblique shocks is governed by both the incoming flow conditions and deflection angle. In cases where the deflection angle is higher than 30°, a dead zone may occur when the incoming Froude number is less than 3.5 (Gray and Cui 2007). The formation of dead zones enhances energy dissipation and attenuates the impact load between the incoming-flow and barrier. For dry granular flows, the prediction of the oblique-shock runup height with dead zones has been investigated by Cui (2021) and Gray and Cui (2007). However, the prediction of oblique-shock impact load for such situation warrants further investigation (Khan et al. 2022).

7. Conclusions

The determination of runup height and impact load of oblique shocks with known incoming-flow conditions is of great significance for design of debris-flow mitigation structures. Based on the conservation of mass and momentum, this study proposes runup height and impact load models for debris-flow oblique shocks against a rigid deflection barrier. These theoretical models are further validated through well-controlled flume experiments. The prediction of shock angle, the formation of dead zone as well as the applicability of proposed models, are also discussed. The key conclusions are as follows:

(1) A model for oblique-shock impact load is proposed. This model takes into account of the hydrodynamic force, hydrostatic force, as well as the gravitational and frictional forces on the control volume, and further decomposes the impact load into two components in the directions parallel and perpendicular to incoming flow. The impact load increases as the incoming-flow Froude number increases, emphasizing the contribution of the hydrodynamic force. Experimental verification confirms that the model well predicts the oblique impact load with known incoming-flow conditions.
(2) The study finds that both runup height and impact load of oblique shocks increase with the incoming Froude

number (1.4–2.9), and are significantly lower than the predictions for normal shocks. Therefore, design based on normal shock predictions would be overly conservative. In particular, the use of normal-shock predictions can lead to deviations of up to 50% compared to those derived from oblique-shock models. Therefore, estimating the runup height and impact load based on oblique-shock models is necessary.

(3) At deflection angle higher than 30°, dead zone would be observed between the barrier and deflected flow. The proposed models are not applicable for oblique shocks with formation of dead zones. It would be beneficial to further explore the theoretical models considering the influence of dead zones.

Acknowledgements

The authors acknowledge the financial support from the National Natural Science Foundation of China (Grant No. 42477193), the Science and Technology Research Program of the Institute of Mountain Hazards and Environment, Chinese Academy of Sciences (Grant Nos. IMHE-JCCX-02 and IMHE-CXTD-02), and the LiaoNing Revitalization Talents Program (XLYC2203149). Support from the Dongchuan Debris Flow Observation and Research Station (DDFORS), Chinese Academy of Sciences is acknowledged.

Article information

History dates

Received: 1 January 2025
Accepted: 16 June 2025
Accepted manuscript online: 8 July 2025
Version of record online: 21 August 2025

Copyright

Data availability

The videos are attached as supplementary files of the manuscript, and other measured data are available upon request to the corresponding author (drsong@imde.ac.cn).

Author information

Author ORCIDs

Dongri Song https://orcid.org/0000-0001-6892-9770

Author contributions

Conceptualization: DS
Investigation: DS, JL
Methodology: YL, JL, LF
Writing – review & editing: YL, JL

Competing interests

The authors declare there are no competing interests.

Supplementary material

Supplementary B1: Debris-flow oblique shock in Jiangjia Ravine.mp4 (https://youtu.be/6GQUBHfEEg8).
Supplementary B2: Side view of typical physical process.mp4 (https://youtu.be/E8gnsdfh6X8).
Supplementary B3: Plan view of typical physical process.mp4 (https://youtu.be/_YSlCx3e9Mo).

References

Albaba, A., Lambert, S., and Faug, T. 2018. Dry granular avalanche impact force on a rigid wall: analytic shock solution versus discrete element simulations. Physical Review E, **97**(5): 052903. doi:10.1103/PhysRevE.97.052903. PMID: 29906957.

Chanson, H. 2004. Applications of the momentum principle: hydraulic jump, surge and flow resistance in open channels. Hydraulics of open channel flow. 2nd ed. Butterworth-Heinemann. pp. 50–93. doi:10.1016/B978-075065978-9/50009-X.

Chanson, H. 2009. Development of the Bélanger equation and backwater equation by Jean-Baptiste Bélanger (1828). Journal of Hydraulic Engineering, **135**(3): 159–163. doi:10.1061/(ASCE)0733-9429(2009)135:3(159).

Chen, Q., Song, D.R., Chen, X.Q., Feng, L., Li, X.Y., Zhao, W., and Zhang, Y.N. 2024. The erosion pattern and hidden momentum in debris-flow surges revealed by simple hydraulic jump equations. Water Resources Research, **60**(11):. doi:10.1029/2023WR036090.

China Geological Disaster Prevention Engineering Association. 2018. Specification of design for debris flow prevention. *(T/CAGHP 021-2018)*.

Choi, C., Ng, C.W.W., Goodwin, S.R., Liu, L., and Cheung, W. 2016. Flume investigation of the influence of rigid barrier deflector angle on dry granular overflow mechanisms. Canadian Geotechnical Journal, **53**(10): 1751–1759. doi:10.1139/cgj-2015-0248.

Cui, X. 2021. Strong oblique shock waves in granular free-surface flows. Physics of Fluids, **33**(8):. doi:10.1063/5.0057700.

Cui, X., and Gray, J.M.N.T. 2013. Gravity-driven granular free-surface flow around a circular cylinder. Journal of Fluid Mechanics, **720**: 314–337. doi:10.1017/jfm.2013.42.

Cui, X., Gray, J.N.T., and Johannesson, T. 2007. Deflecting dams and the formation of oblique shocks in snow avalanches at Flateyri, Iceland. Journal of Geophysical Research: Earth Surface, **112**(F4):. doi:10.1029/2006JF000712.

Faug, T. 2015. Depth-averaged analytic solutions for free-surface granular flows impacting rigid walls down inclines. Physical Review E, **92**(6): 062310. doi:10.1103/PhysRevE.92.062310.

Faug, T. 2021. Impact force of granular flows on walls normal to the bottom: slow versus fast impact dynamics. Canadian Geotechnical Journal, **58**(1): 114–124. doi:10.1139/cgj-2019-0399.

Faug, T., Naaim, M., and Fourriére, A. 2007. Dense snow flowing past a deflecting obstacle: an experimental investigation. Cold Regions Science and Technology, **49**(1): 64–73. doi:10.1016/j.coldregions.2007.01.003.

Gray, J., and Cui, X. 2007. Weak, strong and detached oblique shocks in gravity-driven granular free-surface flows. Journal of Fluid Mechanics, **579**: 113–136. doi:10.1017/S0022112007004843.

Gray, J., Tai, Y.-C., and Noelle, S. 2003. Shock waves, dead zones and particle-free regions in rapid granular free-surface flows. Journal of Fluid Mechanics, **491**: 161–181. doi:10.1017/S0022112003005317.

Hákonardóttir, K.M., and Hogg, A.J. 2005. Oblique shocks in rapid granular flows. Physics of Fluids, **17**(7):. doi:10.1063/1.1950688.

Hákonardóttir, K.M., Hogg, A.J., Batey, J., and Woods, A.W. 2003. Flying avalanches. Geophysical Research Letters, **30**(23):. doi:10.1029/2003GL018172.

Hübl, J., Suda, J., Proske, D., Kaitna, R., and Scheidl, C. 2009. Debris flow impact estimation. In Proceedings of the 11th international symposium on water management and hydraulic engineering, Ohrid, Macedonia. University od Ss Cyril and Methodius, Faculty of Civil Engineering, Skopje, Macedonia. pp. 1–5.

Hungr, O., Morgan, G., and Kellerhals, R. 1984. Quantitative analysis of debris torrent hazards for design of remedial measures. Canadian Geotechnical Journal, **21**(4): 663–677. doi:10.1139/t84-073.

Ippen, A.T. 1951. Mechanics of supercritical flow. Transactions of the American Society of Civil Engineers, **116**: 268–295. doi:10.1061/TACEAT.0006520.

Khan, A., Verma, S., Hankare, P., Kumar, R., and Kumar, S. 2020. Shock–shock interactions in granular flows. Journal of Fluid Mechanics, **884**: R4. doi:10.1017/jfm.2019.988.

Khan, A., Hankare, P., Verma, S., Jaiswal, Y., Kumar, R., and Kumar, S. 2022. Detachment of strong shocks in confined granular flows. Journal of Fluid Mechanics, **935**: A13. doi:10.1017/jfm.2022.5.

Kwan, J.S. 2012. Supplementary technical guidance on design of rigid debris-resisting barriers. Geotechnical Engineering Office, HKSAR Government.

Liu, H., Fan, X., Tian, S., and Deng, X. 2024. Dynamic response of buildings under debris flow impact. Journal of Mountain Science, **21**(5): 1581–1597. doi:10.1007/s11629-023-8572-x.

Mejean, S., Faug, T., and Einav, I. 2017. A general relation for standing normal jumps in both hydraulic and dry granular flows. Journal of Fluid Mechanics, **816**: 331–351. doi:10.1017/jfm.2017.82.

Nagl, G., Hübl, J., and Scheidl, C. 2024. Real-scale measurements of debris-flow run-ups. Landslides, **21**(5): 963–973. doi:10.1007/s10346-023-02204-6.

Ng, C.W., Li, Z., Poudyal, S., De Silva, W., Bhatta, A., and Liu, H. 2024. Experimental and SPH modeling of debris-flow impact on dual rigid barriers with deflector. Journal of Geotechnical and Geoenvironmental Engineering, **150**(5): 04024023. doi:10.1061/JGGEFK.GTENG-12192.

Ng, C.W.W., Bhatta, A., Choi, C.E., Poudyal, S., Liu, H., Cheung, R.W.M., and Kwan, J.S.H. 2022. Effects of debris flow rheology on overflow and impact dynamics against dual-rigid barriers. Géotechnique. 1–14. doi:10.1680/jgeot.21.00226.

Rajaratnam, N. 1967. Hydraulic jumps. In Advances in hydroscience. Elsevier. pp. 197–280.

Rericha, E.C., Bizon, C., Shattuck, M.D., and Swinney, H.L. 2001. Shocks in supersonic sand. Physical Review Letters, **88**(1): 014302. doi:10.1103/PhysRevLett.88.014302.

Song, D., Chen, X., Zhou, G.G.D., Lu, X., Cheng, G., and Chen, Q. 2021a. Impact dynamics of debris flow against rigid obstacle in laboratory experiments. Engineering Geology, **291**: 106211. doi:10.1016/j.enggeo.2021.106211.

Song, D., Chen, X., Sadeghi, H., Zhong, W., Hu, H., and Liu, W. 2023. Impact behavior of dense debris flows regulated by pore-pressure feedback. Journal of Geophysical Research: Earth Surface, **128**(12): e2023JF007074. doi:10.1029/2023JF007074.

Song, D., Zhou, G.G., Chen, X.Q., Li, J., Wang, A., Peng, P., and Xue, K.X. 2021b. General equations for landslide-debris impact and their application to debris-flow flexible barrier. Engineering Geology, **288**: 106154. doi:10.1016/j.enggeo.2021.106154.

Thielicke, W., and Sonntag, R. 2021. Particle image velocimetry for MATLAB: accuracy and enhanced algorithms in PIVlab. Journal of Open Research Software, **9**: 12. doi:10.5334/jors.334.

Tregaskis, C., Johnson, C.G., Cui, X., and Gray, J.M.N.T. 2022. Subcritical and supercritical granular flow around an obstacle on a rough inclined plane. Journal of Fluid Mechanics, **933**: A25. doi:10.1017/jfm.2021.1074.

Wu, Y., Wang, D., Li, P., and Niu, Z. 2023. Experimental investigation of dry granular flows down an inclined channel against a wall-like obstacle of limited width. Acta Geotechnica, **18**(4): 2141–2154. doi:10.1007/s11440-022-01714-2.

Yu, B., and Chu, V.H. 2023. Impact force of roll waves against obstacles. Journal of Fluid Mechanics, **969**: A31. doi:10.1017/jfm.2023.580.

Appendix A

The oblique shock angle β is implicitly given, meaning that for a given deflection angle α, a regression method is required to determine β. Note that eq. 9 is only applicable to oblique shocks with a high incoming-flow Froude number or a small deflection angle. Appendix A presents the functional relationship between the deflection angle, shock angle β, and the incoming Froude number Fr_1. For any given $Fr_1 > 1$, there are two possible solutions for the shock angle β, as long as the wedge angle α is smaller than the detachment angle α_d. The larger β corresponds to a strong shock (dashed curve), while the smaller β corresponds to a weak shock (solid curve). After passing through the strong shock, the downstream Froude number $Fr_2 < 1$, and the flow is subcritical; whereas, after passing through the weak shock, in most cases $Fr_2 > 1$, and the flow is supercritical (Cui et al. 2007; Gray and Cui 2007; Cui 2021). When eq. 9 is not applicable, we propose an empirical relationships for predicting the shock angle based on experimental trends

Fig. A1. (Cited from Cui et al. (2007)) Oblique shock deflection angle curves for $Fr_1 = 1.5, 2, 3, 5, 8, 15, 50, 500, \infty$. The solid curves denote weak shock solutions, and the short-dashed curves denote the strong shock solutions. The transition between them is indicated by a long-dashed curve and corresponds to the detachment angle α_d. The dash-dotted curve represents the $Fr_2 = 1$.

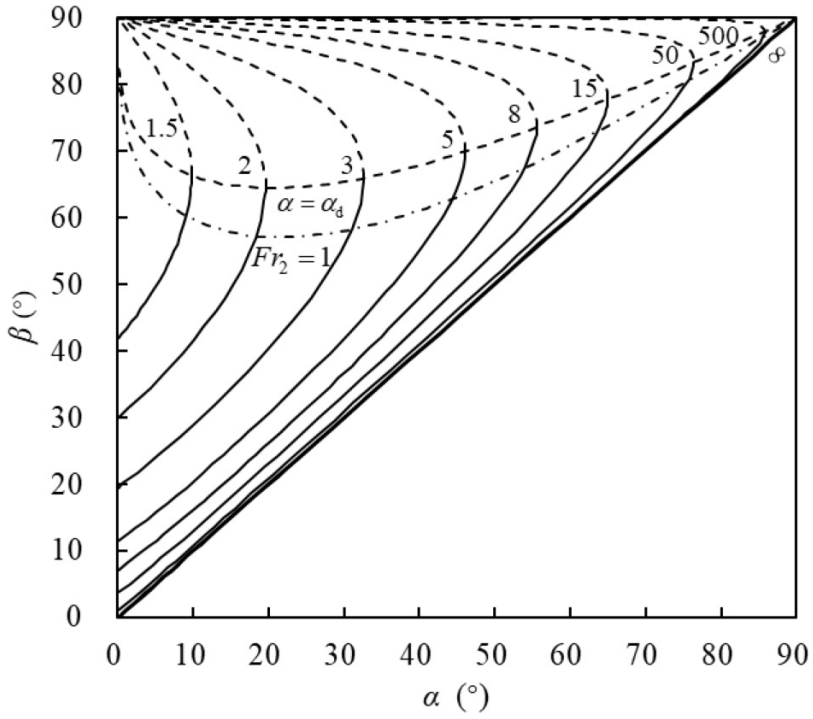

Fig. A2. Incoming-flow velocity of test M-30-30 derived from particle image velocimetry analysis.